IEEE Access
Multidisciplinary | Rapid Review | Open Access Journal

Received January 2, 2021, accepted January 13, 2021, date of publication January 21, 2021, date of current version February 4, 2021.

*Digital Object Identifier 10.1109/ACCESS.2021.3053272*

# Sensor Fault Diagnosis Based on Adaptive Arc Fuzzy DBN-Petri Net

**SHENGLEI ZHAO, JIMING LI, AND XUEZHEN CHENG, (Member, IEEE)**
College of Electrical Engineering and Automation, Shandong University of Science and Technology, Qingdao 266590, China

Corresponding author: Xuezhen Cheng (zhenxc6411@163.com)

This work was supported in part by the National Natural Science Foundation of China Program under Grant 62073198, in part by the Major Research Development Program of Shandong Province of China under Grant 2016GSF117009, and in part by the Minsheng Science and Technology Plan of Qingdao of China Program under Grant 17-3-3-88-nsh.

**ABSTRACT** The adjustable parameters of the traditional fuzzy Petri net (FPN) are single and mostly depend on expert experience. This approach lacks the adaptability to the complex network of sensors, which will result in insufficient accuracy of fault diagnosis. We propose a method combining the FPN with an adaptive arc and deep belief network (DBN) and improved a fast Gibbs sampling (FGS) algorithm to realize sensor fault diagnosis. First, we present the concept of adaptive arcs with label-weights based on the confidence-weights of directed arcs, which is an important component of the sensor fault model. Then, the improved FGS algorithm optimizes the model layer-by-layer, and the adjustment of the transition threshold relies on the marginal distribution of a restricted Boltzmann machine (RBM). Finally, the optimized dual-weights and dual-transition influence factors are applied to the forward and backward fuzzy reasoning of the model to achieve network adaptability. Our studies showed that this method has obvious advantages in terms of the accuracy and adaptability of complex networks compared to other FPN fault diagnosis methods. The fault reasoning confidence can provide an effective reference for maintenance personnel and improve maintenance efficiency, ensuring the reliable operation of sensors and related systems.

**INDEX TERMS** Adaptive arc, fuzzy Petri net, deep belief network, fast Gibbs sampling, sensor fault diagnosis.

## I. INTRODUCTION

As complex detection devices containing multiple components and modules, sensors are susceptible to failure due to external environmental factors and internal factors [1]. Although it can continue working, inaccurate data will affect the control and decision-making of the system, and even bring serious hidden dangers [1], [2]. Early sensor fault diagnosis methods using deviations are usually effective, but excessive use of sensors will increase the cost and make the system more complicated [2]. In addition, although both quantitative analysis and qualitative analysis can realize sensor fault diagnosis [3]–[9], as modern control systems have become more versatile and fault types have become more complex, the previous methods could not meet the current requirements anymore. In recent years, the development of computer technology has provided a new theoretical basis for fault diagnosis technology [2]. The qualitative fault diagnosis based on an expert system is more effective because the complex relationship between the sensor components and the fault characteristics are uncertain and nonlinear. This method does not need to establish an accurate mathematical model but rather analyzes historical data to diagnose whether the sensor is malfunctioning [10]. However, this method has low versatility and scalability [10] and is not suitable for handling inaccurate and uncertain fault information.

The Petri net is a network structure based on the known logical relationships between inputs and outputs in a system, and the place and weight of fuzzy Petri net (FPN) [11] is not limited to the number of tokens, it can express the fuzzy value and has a mechanism for representing and reasoning with uncertain knowledge. The advantage of the FPN is that it can express logical knowledge more intuitively and visually and capture the dynamic nature of fuzzy rule-based reasoning through mark evolution [12], [13]. Unlike traditional expert systems, fuzzy logic can make reasonable decisions under certain and inaccurate situations [12]. The traditional FPN fault diagnosis method [14], [15] is suitable for solving the

The associate editor coordinating the review of this manuscript and approving it for publication was Kathiravan Srinivasan.

problem of unavailability or unreliability of safety data but may lead to insufficient diagnosis accuracy [13]. Furthermore, some FPNs may lack the ability to adjust the parameters, and the setting of weights and transition thresholds depend largely on expert experience, leading to the subjectivity of the diagnosis results.

Endowing the FPN with a certain learning ability in order to improve the adaptability of the network represents a breakthrough in FPN fault diagnosis. To improve the learning ability of the FPN, a generalized fuzzy Petri net (GFPN) was proposed [16]. Due to their powerful nonlinear approximation and adaptive learning capabilities, neural networks have become a widely used nonstatistical data-driven fault diagnosis tool [10]. The adaptive fuzzy Petri net (AFPN) is a model of dynamic knowledge representation and reasoning, and weights are optimized according to the weighted fuzzy production rules (WFPR) [17], endowing the FPN with a learning ability similar to that of neural networks. In [18], the FPN model was established according to the fuzzy production rules in the radar fault expert system; it was combined with a neural network to learn the weights through sample data and then find the cause of the fault through fault reasoning based on the fault probability of the symptom. Li *et al.* [19] focused on the use of neural fuzzy Petri nets (NFPN) combined with an error backpropagation (BP) algorithm for fault diagnosis of corresponding variant sensors, providing confidence-level fuzzy inference formulas and accurately assessing the state of sensors. Tan *et al.* [20] studied a method of power grid fault diagnosis based on intuitionistic fuzzy inhibitor arc Petri net (IFINPN), which aims to simplify the logical relationship of complex networks. Cheng *et al.* [21] considered the learning problem of transition influence factor in FPN, and used the comprehensive learning particle swarm optimization (CLPSO) algorithm to realize fault diagnosis for complex motors.

Previous research has used many approaches to combine the FPN with learning algorithms such as the BP algorithm in parameter optimization [18], [20], [22], [23], with a few studies adopting the Elman, genetic, artificial immune, chaotic bat [24], particle swarm optimization (PSO) [25], and CLPSO algorithms, which mainly solved the problem of fault diagnosis in shallow networks. However, for these methods, the weight and the transition influence factor are singular, the network's mapping ability is limited, the weight convergence speed is slower, it is easy to fall into a local optimum, and the transition threshold generally depends on highly subjective expert experience, which is prone to give low accuracy and poor adaptability of fault diagnosis when faced with a complex fault network [21]. Therefore, to solve the above problems, we propose the DBN-AAFPN fault diagnosis method based on deep belief networks (DBN) [26]–[28]. DBN is a generated graphical model that can be regarded as a deep neural network. Restricted Boltzmann machine (RBM) is a widely used Markov random field (MRF) model, and it is also an important model that constitutes DBN [29]. This model is based on the energy function and can express random neural networks. Therefore, it has a good approximation effect in the face of complex networks and large quantities of data [26]. The fast algorithm of contrast divergence (CD) proposed by Hinton [30] has always been the standard algorithm for training RBM models since the early days. Gibbs sampling is a well-known Markov Monte Carlo (MCMC) algorithm that can extract samples from complex high-dimensional posterior distributions and is often used in randomization algorithms for Bayesian inference [31]. The fast Gibbs sampling (FGS) [29] algorithm based on Gibbs sampling adds acceleration weights and adjustment coefficients, significantly improving the mixing speed of the sampling chain and the accuracy of RBM training. Most of the existing improved FGS algorithms achieve a faster convergence rate at the data and algorithm level to achieve better prediction results [32]–[36]. However, there are relatively few algorithm improvements for complex fault diagnosis models.

This article combines the FPN and DBN to present an adaptive arc generation mechanism that introduces the label-weight based on confidence-weight to mark the occurrence of a fault. The introduction of dual-transition influence factors does not require an artificial setting of transition thresholds, which depend on the marginal distribution of RBM. These two methods combine the improved FGS algorithm to improve the adaptability and accuracy of fault diagnosis. The main contributions of this study are as follows:

- Based on the FPN, we proposed an adaptive arc, dual-weights (label-weight and confidence-weight) and dual-transition influence factors, and obtained a new FPN called adaptive arc fuzzy Petri net (AAFPN).
- Combine the AAFPN and the DBN to form the DBN-AAFPN, which makes it more adaptable than the previous FPN, thereby improving the accuracy of fault diagnosis for complex models.
- We improved the FGS algorithm and applied it to the network optimization of DBN-AAFPN, which achieved better optimization results than other algorithms.

## II. THE PROPOSED METHOD: ADAPTIVE ARC FUZZY DBN-PETRI NET (DBN-AAFPN)

### A. ADAPTIVE ARC FUZZY PETRI NET (AAFPN)

*Definition 1:* The AAFPN is a compound six-tuple:

$$\sum\nolimits_1 = \{S, T, F, A, W(x, y), M\}, \tag{1}$$

where $\{S, T, F, M\}$ is a marked net, $S \cap T = dom(F) \cap cod(F) = \varnothing$, $S \cup T = dom(F) \cup cod(F) \neq \varnothing$, $F \subseteq (S \times T) \cup (T \times S)$, and $M : S \to \{0, 1\}$. Moreover, $A \subset (\cdot T \times S\cdot) \subset F$ is an adaptive arc set, represented by a combination of dotted lines and hollow arrows, as shown in Fig. 1, the dual-weight $W(x, y)$ is composed of the confidence-weight $W(x)$ and the label-weight $W(y)$, where $w(x) \in W(x)$, $0 \leq w(x) < 1$, $w(y) \in W(y)$, $w(y) = 0$ or 1. For $\forall t \in T, \forall s \in S : (s, t) \in F \to M(s) = 1, \forall t \in T, \forall s \in S : (\cdot t \times s\cdot) \in A \to w(y) = 1$, otherwise, $w(y) = 0$. In other words, only when the transition $t$ is enabled can the corresponding adaptive arc be activated.

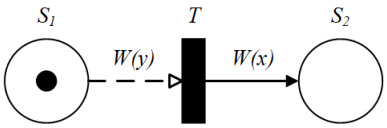


**FIGURE 1.** Adaptive arc fuzzy Petri net.

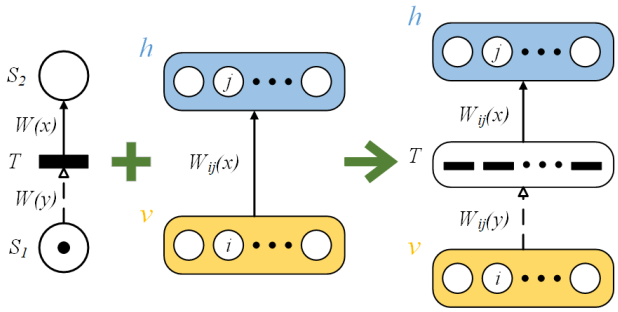


**FIGURE 2.** Adaptive arc fuzzy RBM-Petri net structure.

At this time, the label-weight $w(y)$ of the adaptive arc is set to one; otherwise, it is set to zero.

### B. ADAPTIVE ARC FUZZY RBM-PETRI NET

AAFPN's confidence propagation algorithm is an iterative method that can solve the probabilistic reasoning problem of the complex probability graph model, and all information propagation can be run in parallel to achieve higher computational efficiency. In addition, the DBN formed by stacking RBM is a random neural network with strong self-learning ability. As shown in Fig. 2, the combined adaptive arc fuzzy RBM-Petri net can be regarded as the inference engine in the expert system, and the confidence value of all fault places can be obtained through efficient inference calculation, which can be used as the basis of fault diagnosis [19]. The definition of fuzzy RBM-Petri net is shown in Equation (2).

*Definition 2:* The adaptive arc fuzzy RBM-Petri net is a compound eleven-tuple:

$$\sum\nolimits_2 = \{P, T, I, O, K, W(x, y), v, h, a, b, \lambda\}, \qquad (2)$$

1) $P = (p_1, p_2, \ldots, p_n)^T$ is a collection of faults, including all of the faults related to the sensor.
2) $T = (t_1, t_2, \ldots, t_m)^T$ is a set of transitions, indicating the evolution of the fault. If the transition is enabled, then $t_j = 1$; otherwise, $t_j = 0$.
3) $I$ is the input matrix of the fuzzy RBM-Petri net.
4) $O$ is the output matrix of the fuzzy RBM-Petri net.
5) $K = (k_1, k_2, \ldots, k_n)^T$ represents the label vector of the place. When the fault place occurs, $k_j = 1$; otherwise, $k_j = 0$.
6) $W(x, y) = \{w_{ij}(x), w_{ij}(y)\}$ is the dual-weight matrix between the place and the transition, including the confidence-weight $w(x)$ of the visible layer place and the label-weight $w(y)$ of the hidden layer place. $W(y)$ is an $m \times n$ matrix with only zero or one, $W(x) = (w(x_1), w(x_2), \ldots, w(x_q))^T$, where $q$ depends on the number of visible layer places of the next fuzzy RBN-Petri net and the connection mode with the hidden layer places of this layer.
7) $v = (v_1, v_2, \ldots, v_n)^T$ is the n-dimensional confidence vector of the visible layer place and indicates the credibility of the fault.
8) $h = (h_1, h_2, \ldots, h_m)^T$ is the m-dimensional confidence vector of the hidden layer place and indicates the credibility of the fault.
9) $a = (a_1, a_2, \ldots, a_n)^T$ is the n-dimensional confidence vector of the transition influence factors.
10) $b = (b_1, b_2, \ldots, b_m)^T$ is the m-dimensional confidence vector of the transition influence factors.
11) $\lambda = (\lambda_1, \lambda_2, \ldots, \lambda_n)^T$ is the threshold set of transition vectors and depends on the marginal distribution of RBM.

### C. FUZZY INFERENCE OPERATOR

To clearly express the forward and backward reasoning mechanism of fuzzy RBM-Petri net, four special operators are introduced:

1) The comparison fuzzy operator $\diamondsuit$: $C = A \diamondsuit B$, where $A$, $B$ and $C$ are $m \times n$ matrices. When $a_{ij} \geq b_{ij}$, $c_{ij} = 1$, but when $a_{ij} < b_{ij}$, $c_{ij} = 0$. $i = 1, 2, \ldots, m; j = 1, 2, \ldots, n$.
2) The minimum fuzzy operator $\wedge$: $C = A \wedge B$, where $A$, $B$ and $C$ are $m \times n$ matrices. $c_{ij} = min(a_{ij}, b_{ij})$, $i = 1, 2, \ldots, m; j = 1, 2, \ldots, n$.
3) The maximum fuzzy operator $\vee$: $C = A \vee B$, where $A$, $B$ and $C$ are $m \times n$ matrices. $c_{ij} = max(a_{ij}, b_{ij})$, $i = 1, 2, \ldots, m; j = 1, 2, \ldots, n$.
4) The max-min fuzzy composition operator $\circ$: $C = A \circ B$, where $A$, $B$ and $C$ are $m \times n$ matrices. $\mu_{c_{ij}} = \bigvee_{i=1,j=1}^{m,n} \{\mu_{a_{ij}}(x, y) \wedge \mu_{b_{ij}}(x, y)\}$, $i = 1, 2, \ldots, m; j = 1, 2, \ldots, n$.

## III. DBN-AAFPN CONFIDENCE REASONING

### A. FORWARD REASONING

When the transition connected to the fault place is fired, the corresponding forward propagation path is opened. According to the assumed fault type, forward reasoning can realize the fault location and determine the fault propagation path. The adaptive arc fuzzy RBM-Petri net has $n$ visible places and $m$ hidden places, and vectors $v$ and $h$ represent the states of the visible places and hidden places, as well as the initial confidence and inference confidence of the assumed fault type, as shown in Fig. 2. $v_i$ represents the state of the $i$th visible storage place, and $h_j$ represents the state of the $j$th hidden storage place [19]. Given a set of states $(v, h)$, the energy definition of the adaptive arc fuzzy RBM-Petri net as a system is shown in Equation (3).

$$E = (v, h|\theta) = -\sum_{i=1}^{n} a_i v_i - \sum_{j=1}^{m} b_j h_j - \sum_{i=1}^{n} \sum_{j=1}^{m} v_i w_{ij} h_j \quad (3)$$

In the above equation, $a_i$, $b_j$, and $w_{ij}(x)$ are the parameters of adaptive arc fuzzy RBM-Petri net, where $a_i$ represents the transition influence factor of the visible place unit $i$, $b_j$ represents the transition influence factor the hidden place unit $j$, and $w_{ij}(x)$ represents the confidence weight between the visible layer place and the hidden layer place. When the initial parameters are determined, based on the energy function, the joint probability distribution of $(v, h)$ and its marginal distribution can be obtained [37], as shown in Equations (4) and (5). The marginal distribution represents the distribution of the observation data $v$, which determines the adjustment of the transition threshold $\lambda$ and the firing conditions of the transition, where $Z(\theta)$ is the normalization factor, also known as the partition function.

$$P(v, h|\theta) = \frac{e^{-E(v,h|\theta)}}{Z(\theta)}, \quad Z(\theta) = \sum_{v,h} e^{-E(v,h|\theta)} \tag{4}$$

$$P(v|\theta) = \frac{1}{Z(\theta)} \sum_{h} e^{-E(v,h|\theta)} \tag{5}$$

The adaptive arc fuzzy RBM-Petri net is a special structure with connections between the layers and no connections within the layers. When given the state of visible layer places, the activation states of the hidden layer places are independent of each other. At this time, the activation probability of the $j$th hidden layer place is shown in Equation (6).

$$P(h_j = 1|v, \theta) = \sigma(b_j + \sum_{i} v_i w_{ij}(x)) \tag{6}$$

The structure of the adaptive arc fuzzy RBM-Petri net is symmetric. When the state of the hidden layer place is given, the activation state of each visible layer place is also conditionally independent, and the probability of the $i$th visible layer place is shown in Equation (7).

$$P(v_i = 1|h, \theta) = \sigma(a_i + \sum_{j} w_{ij}(x) h_j) \tag{7}$$

where $\sigma(z) = (1 + exp(-z))^{-1}$ is the *Sigmoid* activation function.

### B. BACKWARD REASONING

Backward reasoning is the process of analyzing the causes of the fault and realizing fault diagnosis. The optimized DBN-AAFPN model is used to obtain the inference confidence and the actual fault type according to the confidence of the terminal fault place obtained from the confidence prediction value of forward reasoning, and the effective recovery of the sensor fault is obtained by combining the fault priority. The method of the max-min and maximum fuzzy composition operation is adopted in backward fuzzy reasoning, as shown in Equations (8) and (9).

$$v^{(l)'} = \left(h^{(l)} \circ W^T(x)\right) \circ W(y) \tag{8}$$

$$h^{(l-1)'} = v^{(l)T'} \vee h^{(l-1)} \tag{9}$$

where $v^{(l)'}$ is the confidence value of the visible layer place of the RBM-Petri net of the $l$th layer of backward reasoning,

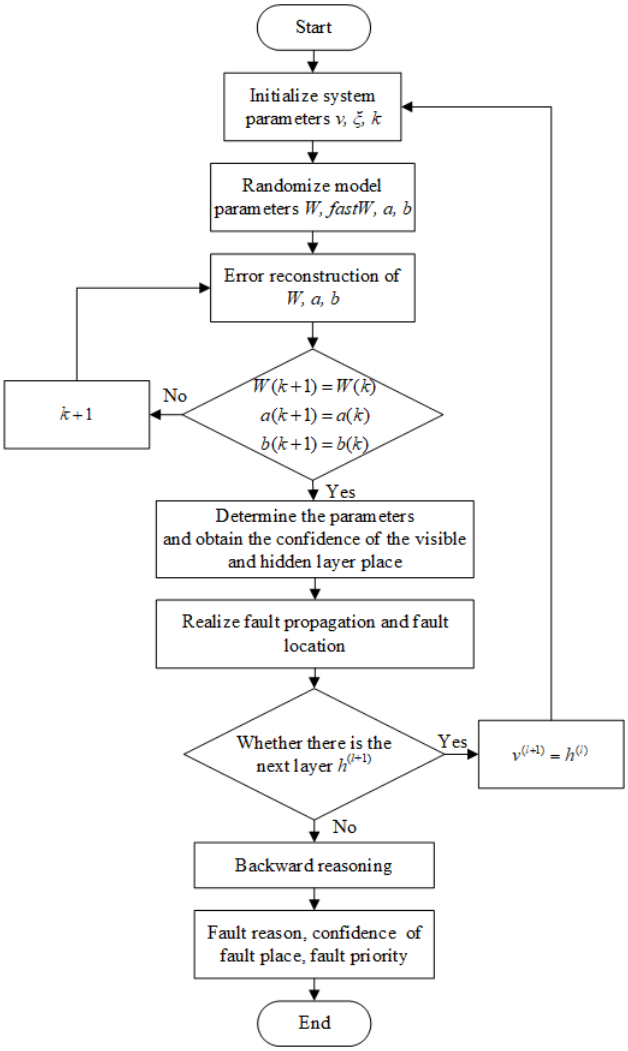


**FIGURE 3.** DBN-AAFPN fault diagnosis process.

and $h^{(l-1)'}$ is the confidence value of the hidden layer place of the $(l-1)$th layer. $h^{(l-1)}$ is the confidence value of the hidden layer place in the $(l-1)$th layer of forward reasoning.

## IV. FAULT DIAGNOSIS

### A. REASONING RULES AND DIAGNOSIS PROCESS

The reasoning rules and process of the DBN-AAFPN fault diagnosis method are shown in Fig. 3.

### B. ESTABLISH FAULT MODEL

In this article, the 3irobotix Delta-2A laser radar is selected as the research object of sensor fault diagnosis, and the DBN-AAFPN fault model is established according to its structural principle and failure mode. The DBN-AAFPN model of laser radar and the corresponding semantics of the places are shown in Appendix A. The laser radar is mainly composed of "laser" and "receiver". To facilitate the analysis, this article selects the "laser fault" local model to illustrate the learning and reasoning process of this method. As shown in Fig. 9, the DBN-AAFPN fault model consists

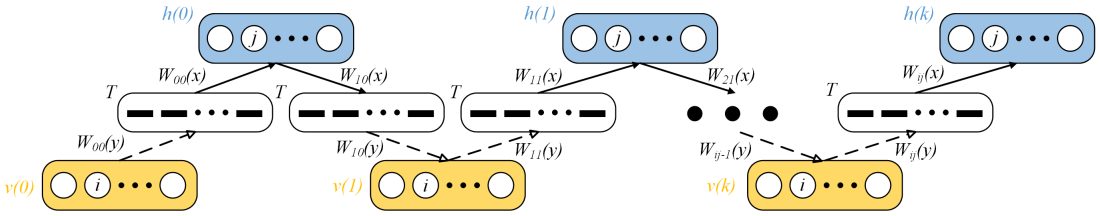


**FIGURE 4.** FGS algorithm learning process.

of three layers stacked by adaptive arc fuzzy RBM -Petri nets.

### C. PROCESSING OF RAW DATA

The original data of the fault source in this article is taken from the $GJB/Z299C - 2006$ and $GB/T37963 - 2019$ Reliability Prediction Handbook for Electronic Equipment. Related calculation formulas and tables are shown in Appendix B. Finally, as shown in Equation (10), the initial confidence value of the fault source is obtained by normalizing the Gaussian function.

$$f(x_0) = e^{-5000\cdot(x_0-0.017)^2} \tag{10}$$

### D. SIMULATION

#### 1) IMPROVED FAST GIBBS SAMPLING (FGS) ALGORITHM

Based on the symmetrical structure of the RBM model and the conditional independence of the neuron states, the Gibbs sampling method can be used to obtain random samples that follow the distribution defined by the RBM. The specific algorithm of $k$step Gibbs sampling is to use a training sample or any randomized state of the visible layer place for alternating sampling, as shown in Fig. 4. The FGS algorithm introduces the accelerated confidence-weight $fastW$ and the adjustment coefficient $\xi$, and the confidence-weights of the entire network are the sum of the acceleration confidence-weights $fastW$ and the traditional confidence-weights, effectively ensuring that the confidence-weights updates are updated rapidly in the early stages of training. The added adjustment coefficient can effectively change the update rate of the accelerated confidence-weights, and the adjustment coefficient changes within the range of zero to one, effectively reducing the trend of accelerated confidence-weights update in the middle and later stages of training [29].

The input data used to obtain the data of the hidden layer places, $v^+ = v^-$, both represent the input data, as shown in Equation (11).

$$\begin{cases} h^- = P(h|v^-, W) \\ h^+ = P(h|v^-, W + fastW) \end{cases} \tag{11}$$

The data of the hidden layer places are obtained through calculation, and the positive and negative gradients of the weights are updated as shown in Equation (12).

$$\begin{cases} W^+ = {v^+}^T h^+ \\ W^- = {v^-}^T h^- \end{cases} \tag{12}$$

The data of the visible layer places can be calculated by the hidden layer places, as shown in Equation (13). The confidence-weights are the sum of traditional confidence-weights and accelerated confidence-weights.

$$\begin{cases} v^- = P(v|h^-, W) \\ v^+ = P(v|h^-, W + fastW) \end{cases} \tag{13}$$

To adapt the fault model to multiple fault types and complex topological structures, this article improves the original FGS algorithm, and the weight update gradient is shown in Equation (14). We multiply the update gradient of the weights by the initial confidence of the visible layer places. On the one hand, unnecessary calculations are avoided and optimization efficiency is improved. On the other hand, the confidence-weights corresponding to the non-faulty places quickly converge to values close to zero, and the corresponding label-weights have also been identified and set, ensuring the accuracy in the analysis of the failure causes in backward reasoning. The initial update gradient of the weights consists of the traditional confidence-weight update and the accelerated confidence-weight update. Moreover, the accelerated update of the accelerated confidence-weights depends on the difference between the expected value of the data and the expected value of the model. The reconstruction gradient of the confidence-weights is described by Equations (15) and (16).

$$W = (W + \Delta W_{ij}) * v_i(0) \tag{14}$$

where

$$W = W^+ + W^- \tag{15}$$

$$\begin{aligned} \Delta W_{ij} &= \langle v_i h_j \rangle_{data} - \langle v_i h_j \rangle_{recon} \\ &= P(h_j = 1|v_i(0)) * v_i(0) - P(h_j = 1|v_i(k)) * v_i(k) \end{aligned} \tag{16}$$

The updating of traditional confidence-weights and accelerated confidence-weights is shown in Equation (17). The update of the accelerated confidence-weights is determined by the adjustment coefficient $\xi$ and the update gradient $\Delta W$

of the confidence-weights.

$$\begin{cases} W = W + \Delta W \\ fastW = \xi * fastW + W \end{cases} \tag{17}$$

In addition, the introduction of the dual-transition influence factors can further improve the adaptability of a complex fault model to multiple fault types compared to the single transition influence factor. Similarly, the FGS algorithm is improved, and the update gradient of the transition impact factor $a$ is multiplied by the initial confidence of the visible layer places. The training process of the dual-transition influence factors $a$ and $b$ is shown in Equations (18) and (19). The reconstruction gradient of the dual-transition influence factors is described by Equations (20) and (21).

$$a_i = (a_i + \Delta a_i) * v_i(0) \tag{18}$$

$$b_j = b_j + \Delta b_j, \tag{19}$$

where

$$\begin{aligned} \Delta a_i &= \langle v_i \rangle_{data} - \langle v_i \rangle_{recon} \\ &= v_i(0) - v_i(k) \end{aligned} \tag{20}$$

$$\begin{aligned} \Delta b_j &= \langle h_j \rangle_{data} - \langle h_j \rangle_{recon} \\ &= P(h_j = 1|v(0)) - P(h_j = 1|v(k)) \end{aligned} \tag{21}$$

### 2) MODEL OPTIMIZATION AND TRAINING

In this study, the initial confidence vector of the fault source places is selected by Equation (10) and is $v^{(1)}(0) = (0.3297, 0, 0.5646, 0.9445, 0, 0.2516, 0, 0.2852)^T$. The confidence-weights and dual-transition influence factors are randomly initialized and are $w_{11}(x)$, $w_{21}(x)$, $w_{32}(x)$, $w_{33}(x)$, $w_{44}(x)$, $w_{54}(x)$, $w_{64}(x)$, $w_{65}(x)$, $w_{75}(x)$, $w_{85}(x)$, $a_1$, $a_2$, $a_3$, $a_4$, $a_5$,$a_6$, $a_7$, $a_8$, $b_1$, $b_2$, $b_3$, $b_4$, and $b_5$. The adjustment coefficient $\xi$ is 0.4, the initial acceleration weight $fastW$ is zero, the transition threshold $\lambda$ is set according to the partition function of the fuzzy RBM-Petri net, and the number of learning iterations $k$ is set to 200.

Figs. 5 and 6 show the change process output by the fault places of the visible and hidden layers, respectively, of the first layer of fuzzy RBM-Petri net. The fault places of the remaining hidden layers are generated iteratively layer by layer. After training, the corresponding converged confidence-weight $w(x)$ is obtained and stored in the vector $W(x)$, and the corresponding label-weight $w(y)$ is stored in the vector $W(y)$. The change process of the confidence-weights of the first-layer fuzzy RBM-Petri net is shown in Fig. 7, and the confidence-weights matrix after training is shown in $W^{(1)}(x, y)$, as shown at the bottom of the next page. The confidence-weights corresponding to the fault places converged rapidly, while the confidence-weights corresponding to the non-faulty places quickly converged to $\varepsilon$, where $\varepsilon \to 0^+$. Similarly, the change process of the transition influence factors of the first-layer fuzzy RBM-Petri net is shown in Figs. 8 and 9. In short, for faulty and non-faulty

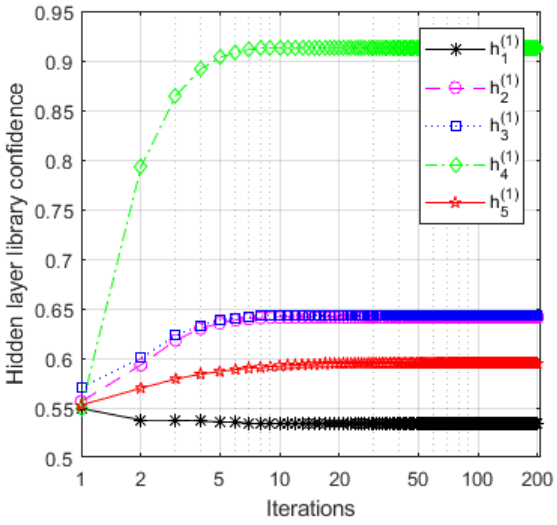


**FIGURE 5.** The change process of the hidden places $h_j$ of the first-layer fuzzy RBM-Petri net.

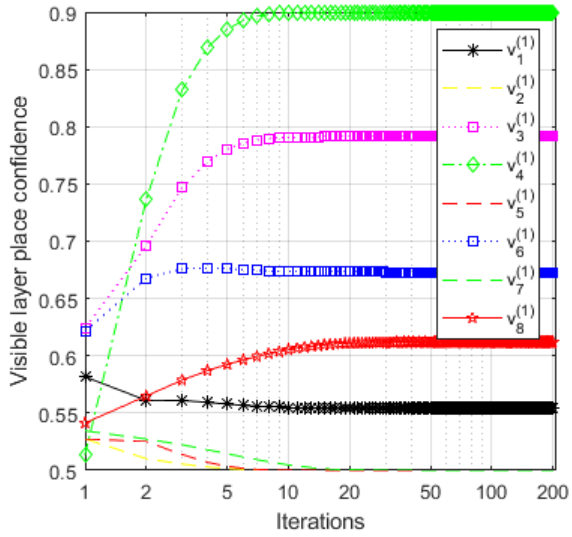


**FIGURE 6.** The change process of the visible places $v_i$ of the first-layer fuzzy RBM-Petri net.

places, various parameters have different convergence properties, which avoids unnecessary calculations and reflects the adaptability of the network.

### 3) FAULT PROPAGATION AND LOCATION

Forward reasoning represents the evolution process from the source of the fault to the end of the fault, from which the location of the fault can be determined, and the location of the fault is represented by the label $K$. The initial confidence $v_0$ is known from the previous text. As shown in Fig. 10, the initial label of the fault source places are $K_1 = (1, 0, 1, 1, 0, 1, 0, 1)^T$, and the corresponding fault modes are "no laser output", "spectral degradation", "drive current increase", "clogged condenser", "crack", "pollution", "unable to adjust", and "electron tube overvoltage".

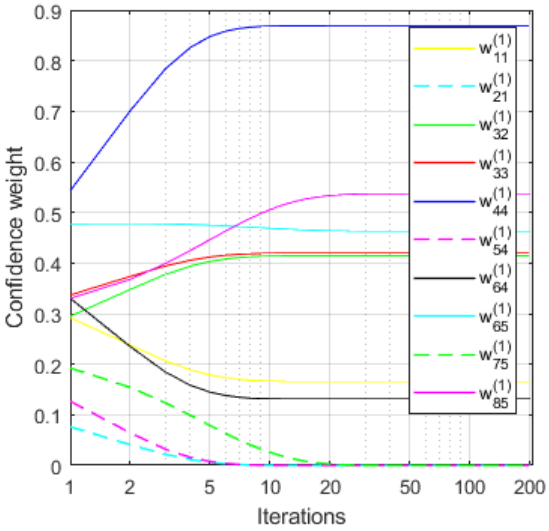


**FIGURE 7.** The change process of the confidence weights $w_{ij}$ of the first-layer fuzzy RBM-Petri net.

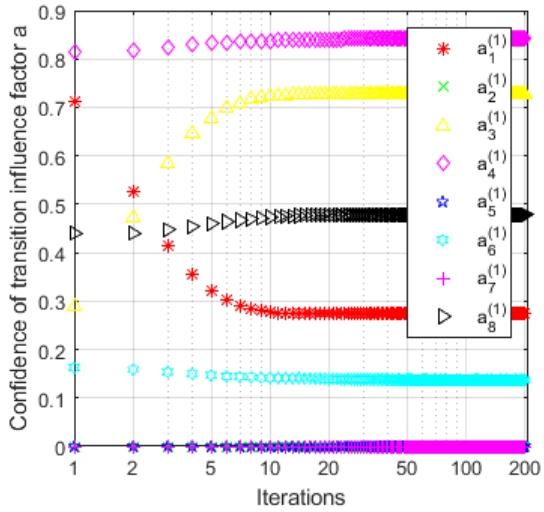


**FIGURE 8.** The change process of the transition influence factors $a_i$ of the first-layer fuzzy RBM-Petri net.

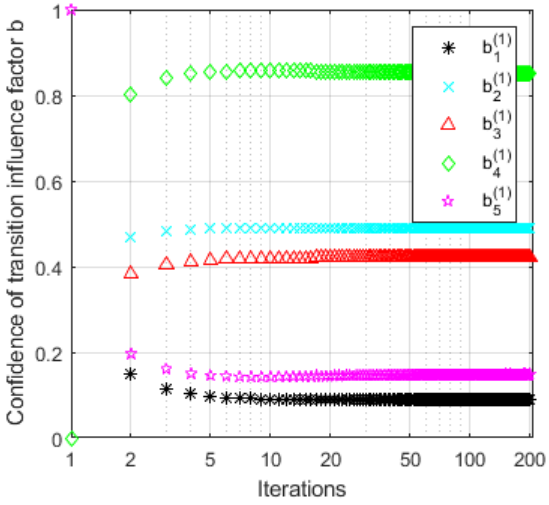


**FIGURE 9.** The change process of the transition influence factors $b_j$ of the first-layer fuzzy RBM-Petri net.

Moreover, the hollow token marks the fault place to be identified.

The improved FGS algorithm is used to obtain the model optimized results as the basis of forward reasoning. The first hidden layer label used as the second visible layer label is $K_2 = (1, 1, 1, 1, 1)^T$, the corresponding failure type is ''laser emission failure'', ''exothermic loss'', ''overcurrent stress'', ''reduced reflectivity'', ''performance failure'', and the place confidence value is $h^{(1)}(k) = v^{(2)}(0) = (0.5340, 0.6415, 0.6432, 0.9135, 0.5948)^T$; the second hidden layer label used as the third visible layer label is $K_3 = (1, 1)^T$, the corresponding failure type is ''optoelectronic semiconductor failure'', ''optical resonant cavity failure'', and the place confidence value is $h^{(2)}(k) = v^{(3)}(0) = (0.6695, 0.6263)^T$; and the third hidden layer label used as the terminal fault place is $K_4 = (1)^T$, the corresponding failure type is ''laser fault'', and the confidence value of the place is $h^{(3)}(k) = (0.6288)^T$.

### 4) FAULT CAUSE ANALYSIS AND DIAGNOSIS

The backward reasoning from the end of the fault to the cause of the fault adopts the inference method of fuzzy composition in turn, as shown in Equations (8) and (9). According to the observed confidence value of the fault end, the corresponding confidence weight $w(x)$ and label weight $w(y)$ are extracted from the pretrained confidence weight vector $W(x)$ and label weight vector $W(y)$. The label of the fault source is obtained through backward reasoning. As shown in Fig. 11, the backward reasoning accurately locates the cause of the fault and obtains the confidence of the relevant fault locations, which can be obtained by the place of the fault marked by

$$W^{(1)}(x, y) = \begin{bmatrix} (0.1659, 1) & (0, 0) & (0, 0) & (0, 0) & (0, 0) \\ (\varepsilon, 0) & (0, 0) & (0, 0) & (0, 0) & (0, 0) \\ (0, 0) & (0.4144, 1) & (0.4196, 1) & (0, 0) & (0, 0) \\ (0, 0) & (0, 0) & (0, 0) & (0.8690, 1) & (0, 0) \\ (0, 0) & (0, 0) & (0, 0) & (\varepsilon, 0) & (0, 0) \\ (0, 0) & (0, 0) & (0, 0) & (0.1310, 1) & (0.4629, 1) \\ (0, 0) & (0, 0) & (0, 0) & (0, 0) & (\varepsilon, 0) \\ (0, 0) & (0, 0) & (0, 0) & (0, 0) & (0.5371, 1) \end{bmatrix}$$

**TABLE 1. Fault related statistics and inference results.**

| Fault Source Place | Initial Confidence | Inference Confidence | | | Number of Faults |
|---|---|---|---|---|---|
| | | Fault Type 1 | Fault Type 2 | Fault Type 3 | |
| $P_1$ | 0.3297 | 0.1659 | - | 0.1659 | 11 |
| $P_2$ | 0.3297 | $\varepsilon$ | - | $\varepsilon$ | 7 |
| $P_3$ | 0.5646 | 0.4196 | - | 0.4196 | 30 |
| $P_4$ | 0.9445 | - | $\varepsilon$ | 0.8690 | 71 |
| $P_5$ | 0.3801 | - | 0.6264 | $\varepsilon$ | 47 |
| $P_6$ | 0.2516 | - | 0.4499 | 0.4629 | 18 |
| $P_7$ | 0.3029 | - | 0.5501 | $\varepsilon$ | 36 |
| $P_8$ | 0.2852 | - | $\varepsilon$ | 0.5371 | 20 |

**TABLE 2. Comparison of different fault diagnosis methods.**

| Method | | AFPN [17] | NFPN [19] | CLPSO-FPN [21] | DBN-AAFPN | DBN-AAFPN |
|---|---|---|---|---|---|---|
| Parameter optimization | | WFPR | BP | CLPSO | FGS [29] | Improved FGS |
| Weight | | Weight | Confidence-weight | Confidence-weight | Confidence-weight, Label-weight | Confidence-weight, Label-weight |
| Transition Influence factor | | - | - | Single transition influence factor | Dual-transition influence factors | Dual-transition influence factors |
| Setting of transition threshold | | Expert experience | Sigmoid function | Gaussian function | Marginal distribution | Marginal distribution |
| Fault diagnosis | Fault Type 1 | $P_{34}$,$P_{35}$,$P_{36}$,$P_{46}$ | $P_{34}$,$P_{35}$,$P_{36}$,$P_{46}$ | $P_{34}$,$P_{35}$,$P_{36}$,$P_{46}$ | $P_{34}$,$P_{35}$,$P_{36}$,$P_{46}$ | $P_{34}$,$P_{35}$,$P_{36}$,$P_{46}$ |
| | Fault Type 2 | $P_{37}$,$P_{38}$,$P_{47}$ | $P_{37}$,$P_{38}$,$P_{47}$ | $P_{37}$,$P_{38}$,$P_{47}$ | $P_{37}$,$P_{38}$,$P_{47}$ | $P_{37}$,$P_{38}$,$P_{47}$ |
| | Fault Type 3 | $P_{34}$,$P_{35}$,$P_{36}$,$P_{37}$, $P_{38}$,$P_{46}$,$P_{47}$ | $P_{34}$,$P_{35}$,$P_{36}$,$P_{37}$, $P_{38}$,$P_{46}$,$P_{47}$ | $P_{34}$,$P_{35}$,$P_{36}$,$P_{37}$, $P_{38}$,$P_{46}$,$P_{47}$ | $P_{34}$,$P_{35}$,$P_{36}$,$P_{37}$, $P_{38}$,$P_{46}$,$P_{47}$ | $P_{34}$,$P_{35}$,$P_{36}$,$P_{37}$, $P_{38}$,$P_{46}$,$P_{47}$ |
| Fault cause | Fault Type 1 | - | $P_1$,$P_3$ | $P_1$,$P_3$ | $P_1$,$P_2$,$P_3$ | $P_1$,$P_3$ |
| | Fault Type 2 | - | $P_5$,$P_6$,$P_7$ | $P_5$,$P_6$,$P_7$ | $P_4$,$P_5$,$P_6$,$P_7$,$P_8$ | $P_5$,$P_6$,$P_7$ |
| | Fault Type 3 | - | $P_1$,$P_3$,$P_4$,$P_6$,$P_8$ | $P_1$,$P_3$,$P_4$,$P_6$,$P_8$ | $P_1$,$P_2$,$P_3$,$P_4$,$P_5$,$P_6$,$P_7$,$P_8$ | $P_1$,$P_3$,$P_4$,$P_6$,$P_8$ |
| Correlation coefficient | Fault Type 1 | - | 0.7946 | 0.8677 | 0.9274 | 0.9667 |
| | Fault Type 2 | - | 0.7523 | 0.8269 | 0.9049 | 0.9540 |
| | Fault Type 3 | - | 0.5962 | 0.6938 | 0.8827 | 0.9266 |

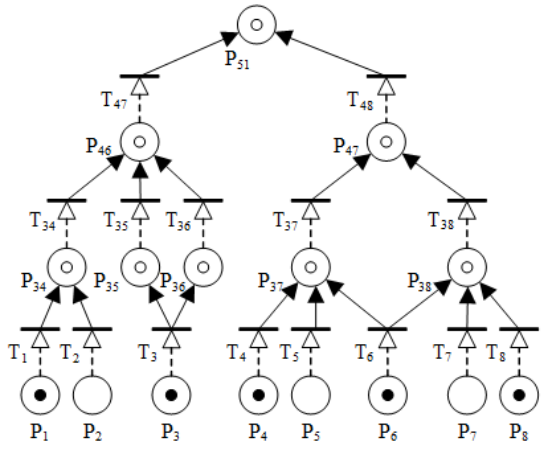


**FIGURE 10. Forward reasoning fault occurrence model.**

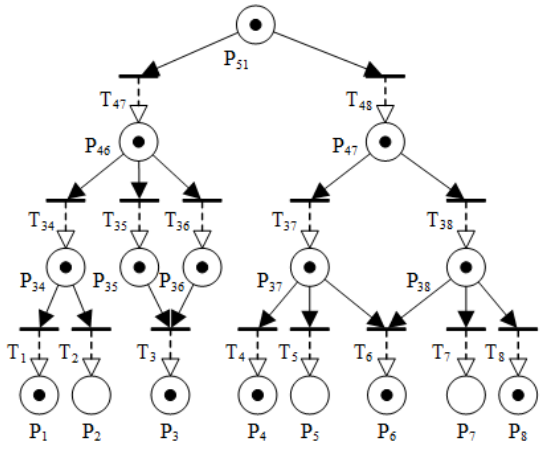


**FIGURE 11. Backward reasoning fault diagnosis model.**

the solid token. This approach provides an effective reference for maintenance personnel and prioritizes maintenance of components with high fault confidence, improving the maintenance efficiency and ensuring the normal operation of the sensor.

After backward reasoning, the confidence value of each layer of the visible layer places and the corresponding fault cause are:

1)

$$K_3' = (1, 1)^T \rightarrow P_{46}, P_{47}$$
$$v^{(3)'} = (0.5187, 0.4813)^T;$$

2)

$$K_2' = (1, 1, 1, 1)^T \rightarrow P_{34}, P_{35}, P_{36}, P_{37}, P_{38}$$
$$v^{(2)'} = (0.2583, 0.3723, 0.3693, 0.6876, 0.3124)^T;$$

3)

$$K_1' = (1, 0, 1, 1, 0, 1, 0, 1)^T \rightarrow P_1, P_3, P_4, P_6, P_8$$
$$v^{(1)'} = (0.1659, \varepsilon, 0.4196, 0.8690, \varepsilon, 0.4629, \varepsilon, 0.5371)^T.$$

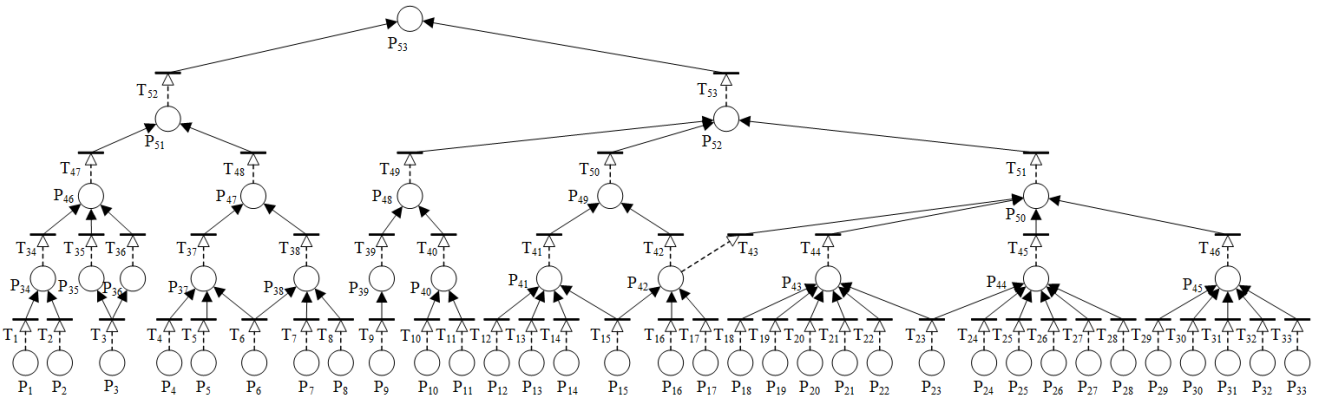

**FIGURE 12.** The DBN-AAFPN fault model of laser radar.

**TABLE 3.** Place semantics of the DBN-AAFPN fault model of laser radar.

| Place | Semantic | Place | Semantic | Place | Semantic |
|---|---|---|---|---|---|
| $P_1$ | No laser output | $P_{19}$ | Electrical over stress | $P_{37}$ | Reduced reflectivity |
| $P_2$ | Spectral degradation | $P_{20}$ | Function failure | $P_{38}$ | Performance failure |
| $P_3$ | Drive current increase | $P_{21}$ | Mechanical failure | $P_{39}$ | Coupling failure |
| $P_4$ | Clogged condenser | $P_{22}$ | Parameter out of tolerance | $P_{40}$ | Line fault |
| $P_5$ | Crack | $P_{23}$ | Measuring open circuit | $P_{41}$ | Performance loss |
| $P_6$ | Pollution | $P_{24}$ | Improper rise time | $P_{42}$ | Connection failure |
| $P_7$ | Unable to adjust | $P_{25}$ | Leakage | $P_{43}$ | Operational amplifier failure |
| $P_8$ | Electron tube overvoltage | $P_{26}$ | No current output | $P_{44}$ | Electronic filter failure |
| $P_9$ | Reduced coupling rate | $P_{27}$ | Electronic filter short circuit | $P_{45}$ | Welding failure |
| $P_{10}$ | Diode short circuit | $P_{28}$ | Switching time failure | $P_{46}$ | Optoelectronic semiconductor failure |
| $P_{11}$ | Diode open circuit | $P_{29}$ | Soldering iron | $P_{47}$ | Optical resonant cavity failure |
| $P_{12}$ | Noise | $P_{30}$ | Fusion welding | $P_{48}$ | Photo-diode failure |
| $P_{13}$ | Functional degradation | $P_{31}$ | Winding | $P_{49}$ | Delay line failure |
| $P_{14}$ | Low radio frequency output | $P_{32}$ | Crimping | $P_{50}$ | Measuring circuit failure |
| $P_{15}$ | Overall degradation | $P_{33}$ | Pinch joint | $P_{51}$ | Laser fault |
| $P_{16}$ | Welding failure | $P_{34}$ | Laser emission failure | $P_{52}$ | Receiver fault |
| $P_{17}$ | Wire fault | $P_{35}$ | Exothermic loss | $P_{53}$ | Laser radar fault |
| $P_{18}$ | Electrical performance failure | $P_{36}$ | Overcurrent stress | | |

**TABLE 4.** Basic failure rate $\lambda_0$ and temperature influence coefficient $\pi_t$.

| Faulty Component | Material | Window $\mu$m | Module Type | $\lambda_0(10^{-9}/h)$ | $\pi_t$ |
|---|---|---|---|---|---|
| Laser diode module | GaAlAs/ GaAs | 0.8 | Basic launch module | 15000 | $\pi_t = e^{4060(\frac{1}{318}-\frac{1}{t_j+273})}$ ($t_j$ is junction temperature, the same below) |
| Laser diode module | InGaAs/ InP | 1.2-1.6 | Basic transmitter module without electronic components | 200 | $\pi_t = e^{4060(\frac{1}{303}-\frac{1}{t_j+273})}$ |
| | InGaAs/ InP | 1.2-1.6 | Transmitting module with electronic components | 300 | |
| | InGaAs/ InP | 1.2-1.6 | Transmitting/receiving module with laser PIN and electronic components, with or without clock recovery function (no crystal components) | 400 | |
| | InGaAs/ InP | 1.2-1.6 | Laser module with integrated modulator | 500 | |
| | InGaAs/ InP | 1.48 | Pump laser module, power≤250mW | 1000 | |
| | InGaAs/ InP | 1.48 | Pump laser module, power>250mW | 1750 | |
| | InGaAs/ GaAs | 0.98 | Pump laser module | 1500 | |
| Photodiode and receiving module for communication | Silicon | 0.7-1.1 | PIN diode | 96 | $\pi_t = e^{4060(\frac{1}{343}-\frac{1}{t_j+273})}$ (Activation energy: 0.35eV) |
| | InGaAs | 0.7-1.1 | PIN diode | 192 | |
| | Silicon | - | APD diode (Avalanche) | 384 | |
| | Germanium | - | APD diode (Avalanche) | 768 | |
| | InGaAs | - | APD diode (Avalanche) | 1536 | |
| | PIN module + electronic components (With or without clock recovery) | | | 576 | |
| | APD module + electronic components (With or without clock recovery) | | | 1920 | |

### *E. STATISTICS AND VERIFICATION*

In this study, the number of faults is taken from the recent five years of statistical data for the laser radar of the intelligent dust removal robot underground in the Huibaoling Iron Mine of Shandong Energy Linyi Mineral Group Co., Ltd. Through backward reasoning, taking a series of specific fault types as an example, we obtain the corresponding confidence of the occurrence of Fault Type 1, Fault Type 2, and Fault

**TABLE 5.** Basic failure rate $\lambda_b$.

| Faulty Component | | $\lambda_b(10^{-6}/h)$ |
|---|---|---|
| Resonator | | 0.14 |
| Magnetic devices | High-power magnetic devices, isolators, amplifiers, gyrators, modulators, circulators, phase shifters, couplers | 0.50 |
| | Low-power magnetic devices (for receivers) | 0.06 |
| Electronic filter | Discrete inductance capacitor | 0.26 |
| | Discrete inductors, capacitors and crystals | 0.58 |
| Welding point | Soldering iron soldering of printed boards | 0.000092 |
| | Welding | 0.0002 |
| | Wrap around | 0.000025 |
| | Crimp | 0.0007 |
| | Clamp | 0.0005 |

**TABLE 6.** Environmental coefficient of the resonator $\pi_E$.

| Environment | $G_B$ | $G_{MS}$ | $G_{F1}$ | $G_{F2}$ | $G_{M1}$ | $G_{M2}$ | $M_P$ | $N_{SB}$ | $N_{S1}$ | $N_{S2}$ |
|---|---|---|---|---|---|---|---|---|---|---|
| $\pi_E$ | 1.0 | 1.2 | 1.5 | 3.5 | 4.0 | 12 | 8.0 | 5.4 | 3.0 | 7.0 |
| Environment | $N_U$ | $A_{IF}$ | $A_{UF}$ | $A_{IC}$ | $A_{UC}$ | $A_{RW}$ | $S_F$ | $M_L$ | $M_F$ | - |
| $\pi_E$ | 14 | 15 | 24 | 10 | 18 | 22 | 1.0 | 32 | 15 | - |

**TABLE 7.** Environmental coefficient of the magnetic devices $\pi_E$.

| Environment | $G_B$ | $G_{MS}$ | $G_{F1}$ | $G_{F2}$ | $G_{M1}$ | $G_{M2}$ | $M_P$ | $N_{SB}$ | $N_{S1}$ | $N_{S2}$ |
|---|---|---|---|---|---|---|---|---|---|---|
| $\pi_E$ | 1.0 | 1.2 | 1.5 | 3.5 | 4.0 | 8.0 | 5.0 | 4.5 | 3.0 | 6.0 |
| Environment | $N_U$ | $A_{IF}$ | $A_{UF}$ | $A_{IC}$ | $A_{UC}$ | $A_{RW}$ | $S_F$ | $M_L$ | $M_F$ | - |
| $\pi_E$ | 12 | 6.5 | 10 | 3.5 | 5.5 | 15 | 1.0 | 22 | 12 | - |

**TABLE 8.** Environmental coefficient of the electronic filter $\pi_E$.

| Environment | $G_B$ | $G_{MS}$ | $G_{F1}$ | $G_{F2}$ | $G_{M1}$ | $G_{M2}$ | $M_P$ | $N_{SB}$ | $N_{S1}$ | $N_{S2}$ |
|---|---|---|---|---|---|---|---|---|---|---|
| $\pi_E$ | 1.0 | 1.2 | 1.5 | 3.5 | 4.0 | 8.0 | 6.0 | 4.0 | 3.0 | 6.0 |
| Environment | $N_U$ | $A_{IF}$ | $A_{UF}$ | $A_{IC}$ | $A_{UC}$ | $A_{RW}$ | $S_F$ | $M_L$ | $M_F$ | - |
| $\pi_E$ | 10 | 9.0 | 14 | 7.0 | 11 | 13 | 0.8 | 25 | 15 | - |

**TABLE 9.** Environmental coefficient of the welding point $\pi_E$.

| Environment | $G_B$ | $G_{MS}$ | $G_{F1}$ | $G_{F2}$ | $G_{M1}$ | $G_{M2}$ | $M_P$ | $N_{SB}$ | $N_{S1}$ | $N_{S2}$ |
|---|---|---|---|---|---|---|---|---|---|---|
| $\pi_E$ | 1.0 | 1.1 | 2.0 | 4.0 | 4.0 | 7.0 | 5.5 | 4.5 | 4.0 | 5.0 |
| Environment | $N_U$ | $A_{IF}$ | $A_{UF}$ | $A_{IC}$ | $A_{UC}$ | $A_{RW}$ | $S_F$ | $M_L$ | $M_F$ | - |
| $\pi_E$ | 10 | 6.0 | 11 | 4.0 | 6.0 | 16 | 1.0 | 25 | 12 | - |

**TABLE 10.** Quality factor $\pi_Q$. (From A to C, the quality is getting lower and lower).

| Quality Level | A | $A_1$ | $A_2$ | B | $B_1$ | $B_2$ | C |
|---|---|---|---|---|---|---|---|
| $\pi_Q$ (Resonator) | - | 0.2 | 0.35 | 1.0 | - | - | 5.0 |
| $\pi_Q$ (Magnetic devices) | 0.35 | - | - | - | 0.65 | 1.0 | 4.5 |
| $\pi_Q$ (Electronic filter) | 0.4 | - | - | 1.0 | - | - | 5.0 |
| $\pi_Q$ (Welding point) | 0.25 | - | - | 1.0 | - | - | 5.0 |

Type 3. The statistical data and inference results are shown in Table 1.

1) Fault Type 1:
Two of the eight fault sources failed, with $P_1$ and $P_3$ faults;
2) Fault Type 2:
Three of the eight fault sources failed, with $P_5$, $P_6$, and $P_7$ faults;
3) Fault Type 3 (Example in this article):
Five of the eight fault sources failed, with $P_1$, $P_3$, $P_4$, $P_6$, and $P_8$ faults.

The Pearson correlation coefficient is a statistical index that measures the actual number of faults and the confidence of inference. The fault correlation calculation can be used as an indicator of fault diagnosis accuracy, and the calculation method is shown in Equation (22). The correlations of the actual faults of the three fault types 1, 2, and 3 are 0.9667, 0.9540, and 0.9266, respectively. Moreover, we have performed comparative experiments for multiple methods under the same defined conditions, including fault model, fault type, network initial parameters, and the number of training iterations. As shown in Table 2, our proposed method has a stronger ability to adjust parameters and a higher adaptability and accuracy of fault diagnosis, and it is consistent with the expected goal.

$$r = \frac{\sum_{i=1}^{n} (x_i - \overline{x})\,(y_i - \overline{y})}{\sqrt{\sum_{i=1}^{n} (x_i - \overline{x})^2 \sum_{i=1}^{n} (y_i - \overline{y})^2}} \tag{22}$$

**TABLE 11. Component failure mode and frequency ratio.**

| Faulty Component | | Failure Mode | | Frequency Ratio |
|---|---|---|---|---|
| Laser | | Clogged condenser | | 42.3% |
| | | Crack | | 9.6% |
| | | Pollution | | 1.2% |
| | | Electronic tube overvoltage failure | | 3.6% |
| | | Helium loss | | 3.6% |
| | | Unable to adjust | | 4.8% |
| | | Cadmium loss | | 34.9% |
| Receiver/ transmitter | | Lead failure | | 17.1% |
| | | Function failure | | 10.0% |
| | | Leakage | | 2.9% |
| | | Microcrack | | 5.7% |
| | | Parameters out of tolerance | | 5.7% |
| | | Short circuit | | 58.6% |
| Laser diode | 1.3 $\mu$m/ 1.55 $\mu$m module (Single mode fiber 9/125) | Diode failure | (1) Spectral degradation (2) Current increase | 10% |
| | | Coupling failure | Significant degradation of output power | 90% |
| | Pump laser module (0.98 $\mu$m,1.48 $\mu$m) | Diode failure | Significant increase in current | 90% |
| | | Coupling failure | Significant degradation of output power | 10% |
| | 0.85 $\mu$m module (Single mode fiber 9/125) | Diode failure | (1) No laser output (2) Spectral degradation (3) Current increase | Module launch: 80% |
| | | Coupling failure | Significant degradation of output power | Module launch:10% |
| | | Broken light | No output power | Module launch:10% |
| Photodiode and receiving module for communication | | Short circuit | | 80% (With window) 40% (With optical fiber) |
| | | Open circuit | | 20% (With window) 10% (With optical fiber) |
| | | Coupling failure | | 0% (With window) 50% (With optical fiber) |
| Operational amplifier | | Electrical performance failure | | 60.0% |
| | | Overvoltage stress | | 9.1% |
| | | Function failure | | 1.5% |
| | | Mechanical failure | | 19.2% |
| | | Open circuit | | 2.1% |
| | | Parameters out of tolerance | | 8.1% |
| Delay line | | Overall degradation | | 28.0% |
| | | Functional degradation | | 22.8% |
| | | Low radio frequency output | | 10.5% |
| | | Noise | | 21.1% |
| | | Welding failure | | 8.8% |
| | | Wire failure | | 8.8% |
| Electronic filter | | Improper rise time | | 31.7% |
| | | Leakage | | 9.3% |
| | | No current out | | 11.0% |
| | | Open circuit | | 15.9% |
| | | Short circuit | | 17.9% |
| | | Switching time failure | | 14.2% |

## V. CONCLUSION

The sensor fault model has a complicated topology and contains a high amount of uncertain information. The adaptability and accuracy of the traditional FPN fault diagnosis method are insufficient. In this research, we presented the concept of adaptive arc and endowed the FPN with the topology and generation mechanism of DBN. The transition threshold does not rely on expert experience but rather on the marginal distribution of RBM, and the dual-weights and dual-transition influence factors are optimized by the improved FGS algorithm, solving the problem of poor diagnostic adaptability caused by the manual setting of parameters and single adjustable parameters. However, a large number of fault source nodes in a complex network will still give rise to high fault information dimensions and node explosion. Therefore, the optimization of fault source nodes is the focus of our next study.

## APPENDIX A

In this article, the 3irobotix Delta-2A laser radar is selected as the research object of sensor fault diagnosis, and the DBN-AAFPN fault model is established according to its structural principle and failure mode, as shown in Fig. 12.

The semantic description corresponding to the DBN-AAFPN fault model places is shown in Table 3.

## APPENDIX B

In this study, we use the standard failure rate and related calculation formulas in the Reliability Prediction Handbook for Electronic Equipment to obtain the original data. The calculation methods of the related failure types and the original data list are shown below. Among them, there are two calculation methods for different types of faults, as shown in Equations (23) and (24). The relevant variables in the formulas, such as basic failure rate $\lambda_0$, temperature influence coefficient $\pi_t$, can be obtained in Table 4 to Table 10, according to the characteristics of the components and actual need. Table 11 shows the proportion of specific failure modes under different failure components, and finally solves the failure rate of specific failure modes through it. In addition, it should be noted that the incomplete failure modes and data in the table can be appropriately adjusted according to work experience.

1) Calculation method of failure rate of laser diode module;
2) Calculating method of failure rate of photodiode and receiving module for communication.
   The 1) and 2) failure rate prediction model is shown in Equation (23).

$$\lambda_a = \lambda_0 \times \pi_t \tag{23}$$

   where $\lambda_a$ is the failure rate, the unit is $10^{-9}/h$, $\lambda_0$ is the basic failure rate of the module, the unit is $10^{-9}/h$, and $\pi_t$ is temperature influence confficient. The values of $\lambda_0$ and $\pi_t$ are shown in Table 4.
3) Calculation method of failure rate of resonator;
4) Calculation method of failure rate of magnetic devices;
5) Calculation method of failure rate of electronic filter;
6) Calculation method of failure rate of welding point.
   The 3) to 6) failure rate prediction model is shown in Equation (24).

$$\lambda_p = \lambda_b \times \pi_E \times \pi_Q \tag{24}$$

   where $\lambda_p$ is the failure rate, the unit is $10^{-6}/h$, $\lambda_b$ is the basic failure rate, the unit is $10^{-6}/h$, and $\pi_E$ is the environmental factor, $\pi_Q$ is the quality factor. The values of $\lambda_b$, $\pi_E$ and $\pi_Q$ are listed in Table 5 to Table 10.

## REFERENCES

[1] N. Bayar, S. Darmoul, S. Hajri-Gabouj, and H. Pierreval, "Fault detection, diagnosis and recovery using artificial immune systems: A review," *Eng. Appl. Artif. Intell.*, vol. 46, pp. 43–57, Nov. 2015.
[2] D. Li, Y. Wang, J. Wang, C. Wang, and Y. Duan, "Recent advances in sensor fault diagnosis: A review," *Sens. Actuators A, Phys.*, vol. 309, Jul. 2020, Art. no. 111990.
[3] Y.-S. Byun, B.-H. Kim, and R.-G. Jeong, "Sensor fault detection and signal restoration in intelligent vehicles," *Sensors*, vol. 19, no. 15, p. 3306, Jul. 2019.
[4] F. Garramiola, J. Poza, P. Madina, J. del Olmo, and G. Ugalde, "A hybrid sensor fault diagnosis for maintenance in railway traction drives," *Sensors*, vol. 20, no. 4, p. 962, Feb. 2020.
[5] D. Zhou, Y. Zhao, Z. Wang, X. He, and M. Gao, "Review on diagnosis techniques for intermittent faults in dynamic systems," *IEEE Trans. Ind. Electron.*, vol. 67, no. 3, pp. 2337–2347, Mar. 2020.
[6] D. Zhou, L. Qin, X. He, R. Yan, and R. Deng, "Distributed sensor fault diagnosis for a formation system with unknown constant time delays," *Sci. China Inf. Sci.*, vol. 61, no. 11, Nov. 2018, Art. no. 112205.
[7] H. Ji, K. Huang, and D. Zhou, "Incipient sensor fault isolation based on augmented mahalanobis distance," *Control Eng. Pract.*, vol. 86, pp. 144–154, May 2019.
[8] J. Shang, D. Zhou, M. Chen, H. Ji, and H. Zhang, "Incipient sensor fault diagnosis in multimode processes using conditionally independent Bayesian learning based recursive transformed component statistical analysis," *J. Process Control*, vol. 77, pp. 7–19, May 2019.
[9] D. Rimpas, A. Papadakis, and M. Samarakou, "OBD-II sensor diagnostics for monitoring vehicle operation and consumption," *Energy Rep.*, vol. 6, pp. 55–63, Feb. 2020.
[10] Z. Gao, C. Cecati, and S. X. Ding, "A survey of fault diagnosis and fault-tolerant techniques—Part II: Fault diagnosis with knowledge-based and hybrid/active approaches," *IEEE Trans. Ind. Electron.*, vol. 62, no. 6, pp. 3768–3774, Jun. 2015.
[11] C. G. Looney, "Fuzzy Petri nets for rule-based decisionmaking," *IEEE Trans. Syst., Man, Cybern.*, vol. 18, no. 1, pp. 178–183, Jan./Feb. 1988.
[12] H.-C. Liu, J.-X. You, Z. Li, and G. Tian, "Fuzzy Petri nets for knowledge representation and reasoning: A literature review," *Eng. Appl. Artif. Intell.*, vol. 60, pp. 45–56, Apr. 2017.
[13] H.-C. Liu, Q.-L. Lin, and M.-L. Ren, "Fault diagnosis and cause analysis using fuzzy evidential reasoning approach and dynamic adaptive fuzzy Petri nets," *Comput. Ind. Eng.*, vol. 66, no. 4, pp. 899–908, Dec. 2013.
[14] M. Gao, M. Zhou, X. Huang, and Z. Wu, "Fuzzy reasoning Petri nets," *IEEE Trans. Syst., Man, Cybern. A, Syst. Humans*, vol. 33, no. 3, pp. 314–324, May 2003.
[15] H. Hu, Z. Li, and A. Al-Ahmari, "Reversed fuzzy Petri nets and their application for fault diagnosis," *Comput. Ind. Eng.*, vol. 60, no. 4, pp. 505–510, May 2011.
[16] W. Pedrycz and F. Gomide, "A generalized fuzzy Petri net model," *IEEE Trans. Fuzzy Syst.*, vol. 2, no. 4, pp. 295–301, Nov. 1994.
[17] X. Li and F. Lara-Rosano, "Adaptive fuzzy Petri nets for dynamic knowledge representation and inference," *Expert Syst. Appl.*, vol. 19, no. 3, pp. 235–241, Oct. 2000.
[18] M. Min, H. Jianguo, and X. H. Shiji, "Research on radar fault diagnosis method based on adaptive fuzzy Petri net," *Chin. J. Sci. Instrum.*, no. 2, pp. 261–265, 2008.
[19] J. Li, X. Zhu, and X. Cheng, "Sensor fault diagnosis based on fuzzy neural Petri net," *Complexity*, vol. 2018, pp. 1–11, Oct. 2018.
[20] M. Tan, J. Li, G. Xu, and X. Cheng, "A novel intuitionistic fuzzy inhibitor arc Petri net with error back propagation algorithm and application in fault diagnosis," *IEEE Access*, vol. 7, pp. 115978–115988, 2019.
[21] X. Cheng, C. Wang, J. Li, and X. Bai, "Adaptive fault diagnosis of motors using comprehensive learning particle swarm optimizer with fuzzy Petri net," *Comput. Informat.*, vol. 39, nos. 1–2, pp. 246–263, 2020.
[22] C. Xuezhen, W. Changan, L. Jiming, and X. Chuannuo, "Motor fault diagnosis based on adaptive neural fuzzy Petri net," *J. Shandong Univ. Sci. Technol., Natural Sci.*, vol. 39, no. 3, pp. 109–117, 2020.
[23] Z. Y. He, J. W. Yang, Q. F. Zeng, and T. L. Zang, "Fault section estimation for power systems based on adaptive fuzzy Petri nets," *Int. J. Comput. Intell. Syst.*, vol. 7, no. 4, pp. 605–614, Jul. 2014.
[24] M. Li, X. Liu, R. Li, R. Zheng, and W. Zhao, "Fault diagnosis of transformer based on chaotic bats algorithm optimizing fuzzy Petri net," in *Proc. 2nd IEEE Adv. Inf. Manage., Communicates, Electron. Autom. Control Conf. (IMCEC)*, May 2018, pp. 885–889.
[25] W.-M. Wang, X. Peng, G.-N. Zhu, J. Hu, and Y.-H. Peng, "Dynamic representation of fuzzy knowledge based on fuzzy Petri net and genetic-particle swarm optimization," *Expert Syst. Appl.*, vol. 41, no. 4, pp. 1369–1376, Mar. 2014.
[26] N. Zhang, S. Ding, J. Zhang, and Y. Xue, "An overview on restricted Boltzmann machines," *Neurocomputing*, vol. 275, pp. 1186–1199, Jan. 2018.
[27] G. E. Hinton, "Reducing the dimensionality of data with neural networks," *Science*, vol. 313, no. 5786, pp. 504–507, Jul. 2006.
[28] G. E. Hinton, S. Osindero, and Y.-W. Teh, "A fast learning algorithm for deep belief nets," *Neural Comput.*, vol. 18, no. 7, pp. 1527–1554, Jul. 2006.
[29] Q. Wang, X. Gao, K. Wan, F. Li, and Z. Hu, "A novel restricted Boltzmann machine training algorithm with fast Gibbs sampling policy," *Math. Problems Eng.*, vol. 2020, pp. 1–19, Mar. 2020.

[30] G. E. Hinton, "Training products of experts by minimizing contrastive divergence," *Neural Comput.*, vol. 14, no. 8, pp. 1771–1800, Aug. 2002.
[31] F. Li, X. Gao, and K. Wan, "Research on RBM training algorithm with dynamic Gibbs sampling," *Acta Automatica Sinica*, vol. 42, pp. 931–942, 2016.
[32] S. He, H.-S. Shin, and A. Tsourdos, "Distributed multiple model joint probabilistic data association with Gibbs sampling-aided implementation," *Inf. Fusion*, vol. 64, pp. 20–31, Dec. 2020.
[33] N. Madani and T. Bazarbekov, "An enhanced conditional co-Gibbs sampler algorithm for data imputation," in *Proc. Comput. Geosci.*, 2020, Art. no. 104655.
[34] J. Lu, J. Zhang, and J. Tao, "Slice–Gibbs sampling algorithm for estimating the parameters of a multilevel item response model," *J. Math. Psychol.*, vol. 82, pp. 12–25, Feb. 2018.
[35] L. Martino, V. Elvira, and G. Camps-Valls, "The recycling Gibbs sampler for efficient learning," *Digit. Signal Process.*, vol. 74, pp. 1–13, Mar. 2018.
[36] R. Alhamzawi, A. Alhamzawi, and H. T. M. Ali, "New Gibbs sampling methods for Bayesian regularized quantile regression," *Comput. Biol. Med.*, vol. 110, pp. 52–65, Jul. 2019.
[37] L. Li, X. Sheng, B. Du, Y. Wang, and B. Ran, "A deep fusion model based on restricted Boltzmann machines for traffic accident duration prediction," *Eng. Appl. Artif. Intell.*, vol. 93, Aug. 2020, Art. no. 103686.

**SHENGLEI ZHAO** is currently pursuing the M.Sc. degree with the College of Electrical Engineering and Automation, Shandong University of Science and Technology. His research interests include sensor fault diagnosis, deep learning, fuzzy reasoning, and Petri net theory and modeling.

**JIMING LI** is currently pursuing the Ph.D. degree with the College of Electrical Engineering and Automation, Shandong University of Science and Technology. His research interests include signal processing, inspection technology, and system integration.

**XUEZHEN CHENG** (Member, IEEE) is currently a Professor with the College of Electrical Engineering and Automation, Shandong University of Science and Technology, Qingdao, China, where she is also the Director of the Automation Department. Her research interests include power system automation, inspection technology and system integration, and information and image processing. She has led and participated in more than ten research projects at the national and provincial levels. She is also a China Postdoctoral Fund Committee Project Reviewer and a China Energy Society Expert.